Computers in Biology and Medicine 107 (2019) 58–72

Contents lists available at ScienceDirect

Computers in Biology and Medicine

journal homepage: www.elsevier.com/locate/compbiomed

Automatic IVUS lumen segmentation using a 3D adaptive helix model

Abdelaziz Hammouche[a,d,e,*], Guy Cloutier[b], Jean-Claude Tardif[c], Kamal Hammouche[d], Jean Meunier[e]

[a] Department of Electrical Engineering, Faculty of Technology, University of M'sila, B.P 166 Ichbilia M'sila, Algeria
[b] University of Montreal Hospital Research Center, Montreal, QC, H2L 2W5 Canada
[c] Montreal Heart Institute, Montreal, QC H1T 1C8 Canada
[d] Laboratoire Vision Artificielle et Automatique des Systèmes, Université Mouloud Mammeri, Tizi-Ouzou, Algeria
[e] Department of Computer Science and Operations Research, University of Montreal, Montreal, QC, H3T 1J4 Canada

ARTICLE INFO

Keywords:
Segmentation
Helix
Active contour
3-D imaging
Speckle
IVUS
Femoral
Coronary

ABSTRACT

In this paper, we develop a three dimensional (3D) segmentation algorithm of the lumen visualized using intravascular ultrasound (IVUS) imaging. These images are known for their various granular textures (speckles) that make the discrimination of different tissues very difficult, especially as a result of the presence of artifacts and shadows generated by tissue calcification. Our model consists of a helical active contour initialized automatically over the sequence, that evolves based on the analysis of the Rayleigh distribution of gray levels in order to extract the luminal border. This novel algorithm is fast, uses an adaptive simple space curve for 3D extraction of the lumen, and is fully automatic. Consequently, it does not require an initialization close to the lumen border. Segmentation was carried out on 19 IVUS sequences with a total of 8918 images acquired in vivo on nine femoral and ten coronary arteries using a 20 MHz probe. These sequences showed many difficulties, such as severe stenosis, bifurcations, side vessels, shadows, and other artifacts. The quantitative evaluation of our algorithm compared to the ground truth for the femoral and coronary datasets showed an overlap greater than 89% for the Jaccard index and greater than 94% for the Dice index, yielding an accuracy of more than 98.5%. Several other metrics are also presented that confirm the efficiency of our helix model compared to other recent methods reported in the literature using a similar ultrasound probe.

1. Introduction

According to Ref. [1], cardiovascular diseases (CVDs) are the leading cause of death globally. An estimated 17.9 million people died of CVDs in 2016, representing 31% of all deaths. A frequent cardiovascular disease is atherosclerosis in which plaque (made of fat, cholesterol, calcium and other substances) develops in artery walls. Plaque can cause a heart attack by severely reducing or stopping the blood flow through an artery. Moreover, plaque can rupture and form blood clots capable of blocking arteries. The investigation of the severity of atherosclerosis is therefore very important for the diagnosis of patients and the development of a therapeutic strategy (medication, bypass surgery, angioplasty [dilation] with or without a stent). For this purpose, intravascular ultrasound (IVUS) produces images of artery cross-sections, providing helpful information about the health of the vessel. To acquire IVUS images, a miniaturized ultrasonic transducer at the end of a catheter is inserted into the artery lumen, brought beyond the lesion of interest, and then slowly withdrawn manually or automatically at a constant speed to image a sequence of equidistant vessel cross-sections. IVUS produces echographic images (Fig. 1) showing cross-sections of arteries that reveal the lumen, walls, and plaque. Given that a typical IVUS exam results in several hundred images per patient, which can be of poor quality due to speckle noise, ring-down artifacts (ultrasound reverberation, Fig. 1d), or shadows (Fig. 1c) in the images, IVUS data are hard to analyze quantitatively.

In the past, many IVUS image segmentation techniques have been reported in order to facilitate the identification of different regions of the artery. Some techniques use a graph-search algorithm based on the image gradient and a priori information on the edge orientation [2–5]. However, these methods were not suficiently accurate for clinical practice and were limited to a succession of two-dimensional (2D) segmentations. A 3D model with new cost functions was proposed in Refs. [6,7]. This model was later improved by Downe et al. [8], who used sliding windows for principal component analysis- (PCA-) based

* Corresponding author. Department of Electrical Engineering, Faculty of Technology, University of M'sila, B.P 166 Ichbilia M'sila, Algeria.
E-mail addresses: hammouchea@hotmail.com (A. Hammouche), guy.cloutier@umontreal.ca (G. Cloutier), Jean-Claude.Tardif@icm-mhi.org (J.-C. Tardif), kamal_hammouche@yahoo.fr (K. Hammouche), meunier@iro.umontreal.ca (J. Meunier).

https://doi.org/10.1016/j.compbiomed.2019.01.023
Received 2 August 2018; Received in revised form 23 January 2019; Accepted 24 January 2019
0010-4825/

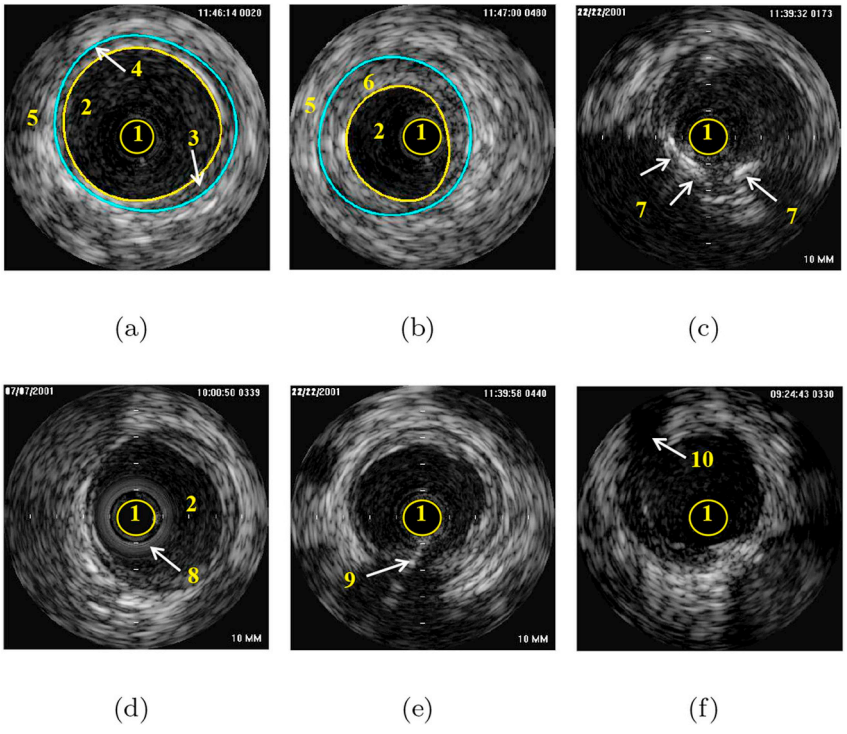

Fig. 1. Cross-sections of IVUS images. (a) Healthy artery, (b–c) Diseased arteries, (d–e) Arteries with artifacts, (f) Arteries with bifurcation: 1- Catheter, 2- Lumen, 3- Intima, 4- Media, 5- Adventitia, 6- Athero-plaque, 7- Tissue calcification, 8- Ring-down artifact, 9- Guidewire artifact, and 10- Bifurcation.

filtering, an active contour for initial segmentation, followed by graph-search segmentation and, eventually, an interactive re-segmentation to refine the results. Recently, Sun et al. [9] proposed a method based on Layered Optimal Graph Image Segmentation of Multiple Objects and Surfaces (LOGISMOS) with computer-aided refinement for the improvement of the segmentation result.

Using the framework of IVUS segmentation based on active contours or snakes, several methods using bi-dimensional parametric, geometric, geodesic, and region-based active contours (fast-marching method) have been developed [10–13]. An extension to 3D active contour methods based on local properties of the image gradient and image intensity have also been developed to successfully extract contours in IVUS sequences [14–16]. Likewise, our group has developed a level set approach to detect IVUS-relevant regions based on a mixture of Rayleigh probability distribution [17]. This method was enhanced by a combination of gray level probability density functions and the intensity gradient embedded in the interface speed function [18]. Unal et al. [19] proposed a statistical shape-driven approach in which the shape evolved by the estimation of the non-parametric probability distributions computed with Parzen windows instead of Rayleigh distributions.

Artificial intelligence (AI) and supervised learning techniques are also used for IVUS segmentation and interpretation [20–24]. A multi-agent system designed for high-level knowledge-based control of low-level image segmentation algorithms was elaborated in Ref. [20]. This system uses six agents specialized in the detection of the lumen, vessels, calcified plaque, shaded branches, and the overall status in order to segment IVUS images. Olszewski et al. [21] proposed a fully automated segmentation that mimics the procedure performed by human experts. Another machine learning algorithm based on artificial neural networks (ANN) was also proposed for the detection of lumen and media-adventitia (MA) in Ref. [22]. This algorithm includes a double structure of ANN in which the first network classifies the pixels roughly while the second ANN optimizes the results of the first network. Finally, an active contour model is applied to smooth both the lumen and MA borders. Lo Vercio et al. [24] defined several feature detectors and applied a Support Vector Machine (SVM) classifier to assign pixels to an arterial area. Sequential feature selection was performed using the area under the precision-recall curve (AUC-PR) in order to select relevant features. Mendizabal-Ruiz et al. [23] proposed a probabilistic approach for the segmentation of the lumen border in IVUS images based on the deformation of a parametric curve via minimization of a probabilistic cost function. The likelihood of each pixel belonging to the lumen was determined by a Support Vector Machine (SVM) trained on the first frame of the sequence. Recently, deep learning architectures designed specifically for biomedical image segmentation have also been introduced [25,26]. They have significant potential, but more development is needed to assess their full utility in IVUS segmentation.

Gao et al. [27] developed an automated framework using an unsupervised clustering and adaptive region-growing for detecting lumen and media-adventitia borders separately. Recently, Jodas et al. [28] used a combination of many algorithms to extract the lumen border, which involved a Gaussian pyramid that reduced the resolution of the input image, K-means and subtractive clustering algorithms that separated the regions of the image according to the grayscale intensity, a convex hull algorithm to identify the lumen region, and a refinement of the lumen contour using an active contour approach with a post-processing step. Faraji et al. [29] extracted the lumen and media-adventitia in four steps. They began by a preprocessing step to remove artifacts. Then, they applied a region detector called EREL (Extremal Regions of Extremum Levels) followed by a region selection strategy to extract the contours of the lumen and media. Finally, these contours were smoothed by an ellipse fitting algorithm. Moraes and Furuie [30] used the polar domain and combined pre-processing and feature extraction involving discrete wavelet packet frames (DWPF) for an automatic segmentation. Finally, a binary morphological image reconstruction and a contour extraction were used to detect the lumen and media-adventitia contours. Haas et al. [31] used an algorithm based on the optimization of a Maximum-A-Posteriori (MAP) estimator, implementing the Rayleigh distributions of speckles and a priori information about the contours to segment IVUS images.

A state-of-the-art review and survey of segmentation algorithms

used in IVUS imaging can be found in Refs. [32–34].

All of these methods suffer from one or several drawbacks. For instance, some of them operate only on 2D images. Others are complex to implement with dynamic 3D meshes or propagating surfaces with cumbersome initialization, while others use a combination of many methods [28]. Most of these methods use a pre-processing step. Some authors allow an interaction with the user for refinement of the segmentation result [8,9]. To simplify the extraction of the region boundaries in IVUS images, our group has previously introduced a space curve active contour segmentation technique with a helical geometry that evolves until it reaches the artery lumen [35]. The algorithm uses simple global properties of the image and facilitates a full 3D reconstruction without heavy techniques involving 3D meshes, propagating interfaces, etc. However, it is less accurate than these state-of-art methods and requires good initialization.

The lumen segmentation technique developed in this paper greatly improves upon our previous work [35]. The 3D active contour is more flexible, fully automatic, and does not require an initialization close to the lumen boundary with a priori displacement direction. The model is an adaptive helicoidal space curve with easy adjustment of the number of turns. Moreover, the evolution of the 3D contour is based on Rayleigh (instead of basic Gaussian) textural properties of the image estimated with radial 3D cubic windows. Finally, a simple pre-processing step is introduced to remove the ring-down artifact and catheter calibration marks.

This paper is also a substantial extension of our preliminary work in Ref. [36], employing an improved methodology (e.g., automatic and adaptive models, 3D windows, improved a priori displacement, more explanations and justifications), better experimental results with additional femoral sequences, a new dataset of coronary sequences, and more evaluation criteria.

2. Method

The method we developed is carried out in four steps. After a pre-processing step to reduce the effect of the ring-down artifact, we initialize our helix snake for the detection of the lumen border. Then, in a key step, the algorithm deforms the helix toward the luminal border by minimizing an energy function. At the end of the segmentation process, we proceed to the 3D reconstruction of the lumen.

2.1. Pre-processing step

The greatest difficulty encountered in the process of segmentation of IVUS images is the presence of artifacts; in particular, the ring-down artifact (Fig. 2 b). This artifact is constant over the entire length of the sequence (Fig. 2 a) and has high gray level intensities, which, in some cases, distorts the segmentation results. This is especially the case when the walls of the intima are close to the catheter. To reduce or eliminate the effect of the ring-down artifact, we use the technique proposed in Ref. [19], which consists of calculating a minimal image I_{min} on a set of frames $\{I_i\}$, $i = 1, \cdots, \lambda$. In this paper, the minimal image is computed from the whole length of the sequence such that every pixel with the coordinates (x, y) of the minimal image $I_{min}(x, y)$ is computed using the following formula:

$$I_{min}(x, y) = \min_{i \in \lambda} I_i(x, y). \tag{1}$$

Then, we subtract the minimum image from all the images in the sequence as follows:

$$I'_i(x, y) = I_i(x, y) - I_{min}(x, y),\ i = 1, \cdots, \lambda. \tag{2}$$

Fig. 2c shows an example of a longitudinal view of a sequence after artifact removal by this pre-processing. Notice that annoying calibration marks are also removed at the same time.

2.2. 3D-helical snake segmentation method

Introduced by Kass et al. [37], the parametric active contour (a.k.a. snake) is one of the most popular algorithms in image processing. Our snake model, consists of a three-dimensional spiral space curve similar but more flexible than the one proposed in Ref. [35]. This helical snake is constituted of a set V of N control points, where each point $v_i \in V$, $i = 1, \cdots, N$ is radially moved in order to minimize the energy function, noted E_S:

$$E_S(V) = \sum_{i=1}^{N} \left(\alpha E_{int}(v_i) + \left(1 - \alpha\right) E_{ext}(v_i) \right), \tag{3}$$

where α is a weighting parameter adjusted by the user. The energy of the snake is the sum of two terms. The first term represents the internal energy, noted E_{int}, which depends on the geometrical properties of the model such as continuity and curvature and which manages the regularity of the snake shape. The second term represents the external energy, noted E_{ext}, calculated from local gray level distributions.

2.2.1. Automatic 3D-helical snake initialization

The three-dimensional helical snake is initialized on the whole sequence, where each complete helix turn is constituted of a set of points. Each point $v_i \in V$, $i = 1, \ldots, N$ evolves until it coincides with the lumen contour. It is defined by the Cartesian coordinates [38]:

$$\begin{cases} x(v_i) = r_i \cos(\theta_i) \\ y(v_i) = r_i \sin(\theta_i) \\ z(v_i) = z_i \end{cases}, \tag{4}$$

where r_i, θ_i and z_i are respectively the radius, the angular position and the axial length (or height) of the spiral at the point v_i.

The helical snake is automatically initialized over the sequence by the generation of a centered helix model with a radius equal to 2 mm. The number of points and the number of turns can be chosen beforehand by a user according to the length of the sequence and smoothness of the luminal border[1]. Fig. 3 shows an example of the initial 3D helical snake. Since the points $v_i(x_i, y_i, z_i)$ are radially moved, they will be represented by cylindrical coordinates $v_i(r_i, \theta_i, z_i)$, which correspond to the radial positions, angular positions and depth in the sequence, respectively.

2.2.2. Helical snake energies

For each helical snake point $v_i(r_i, \theta_i, z_i)$, the algorithm searches for a new position that minimizes the energy function defined by equation (3). A point of the snake is radially moved in a neighborhood of points (potential future position) $w_j \in W$, with $W = W_{in} \cup W_{out}$, where W_{in} and W_{out} represent respectively the neighborhood inside and outside of the current contour with the same angular position θ_i and the same depth z_i of the control points v_i.

In this subsection, we define the internal energy and the external energy used to compute the potential future position.

2.2.2.1. Internal energy. To ensure a smooth curve and to maintain the cohesion of the points and the rigidity of the curve, we followed the same idea proposed by Ref. [39] and adapted by Ref. [35]. The internal energy is related to the difference in radial positions between consecutive points v_i, v_{i-1} and v_{i+1} of the snake [36]. This energy is minimal if the helix is circular as expected for a normal lumen. It is defined as follows:

$$E_{int}(v_i) = \sqrt{(r_i - r_{i-1})^2 + (r_i - r_{i+1})^2}\ , \tag{5}$$

where r_i , r_{i-1} and r_{i+1} are respectively the radial coordinates of the points v_i, v_{i-1} and v_{i+1}.

[1] More (less) points and/or turns also involve more (less).

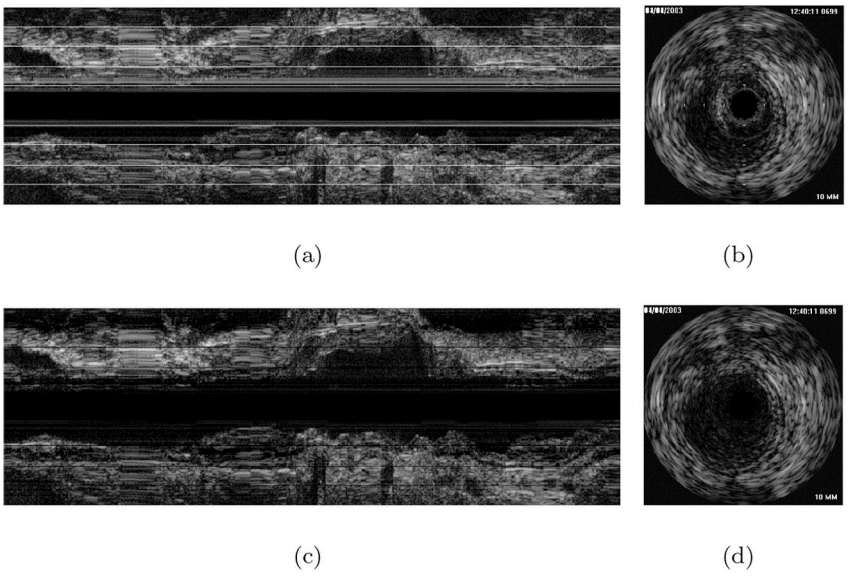

Fig. 2. Ring-down artifact and catheter calibration marks removal. (a) A longitudinal view of the original sequence, (b) Original IVUS frame, (c) A longitudinal view of the sequence after artifact removal, (d) IVUS frame after artifact removal.

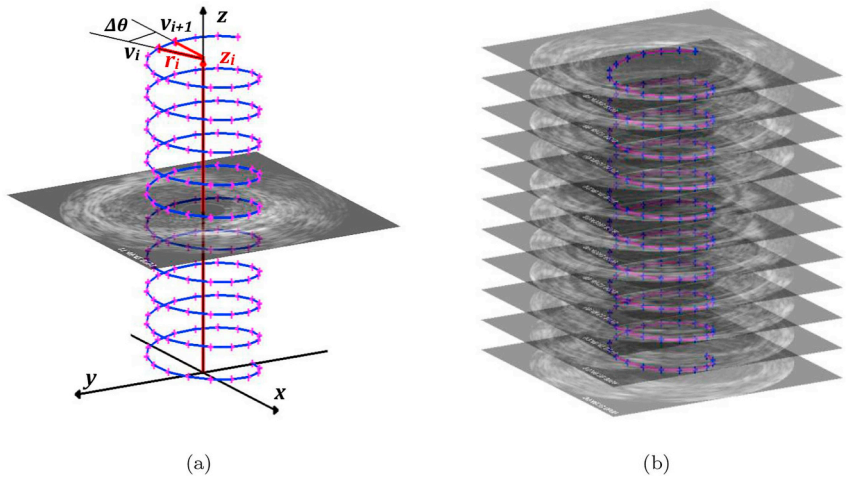

Fig. 3. Initialization of the 3D helical snake. (a) The helix model, (b) Helix snake Initialized over the IVUS sequence.

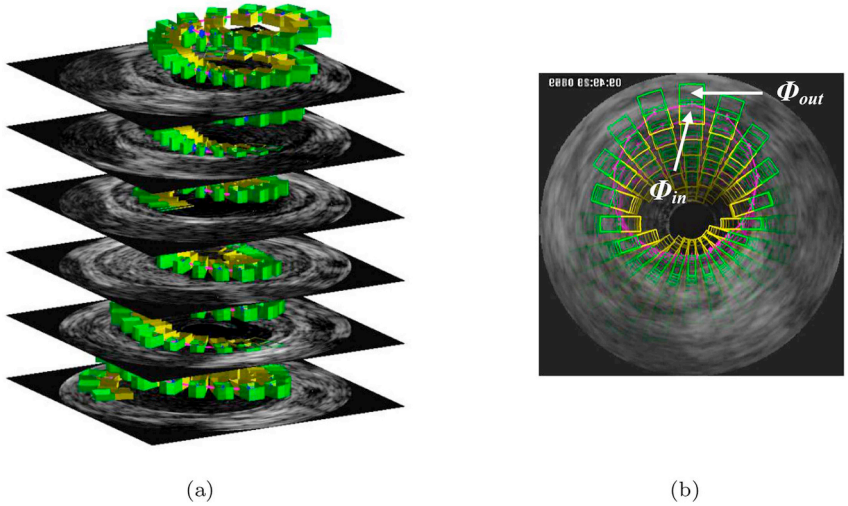

Fig. 4. (a) Selection of cubic windows, inside (yellow) and outside (green) for each point of the snake. (b) Top view.

2.2.2.2. External energy. The external energy corresponds to the adequacy of the helical snake with the image data (gray level distributions). The minimization of this energy attracts the snake towards the lumen boundary with highest likelihood (i.e. lumen on one side and tissue on the other side) similarly to the likelihood energy proposed by Mignotte et al. [40] and later adapted by Refs. [35,36]. To compute the proposed external energy term, for each point v_i, we select two radial cubic windows $\phi_{in}(v_i)$ and $\phi_{out}(v_i)$ that contain, respectively, the cubic neighborhood inside and outside of the point v_i as illustrated in Fig. 4.

The external energy term takes into account the gray level Rayleigh distributions to seek the minimum sum of the negative log-likelihood of the inside ϕ_{in} and outside ϕ_{out} windows:

$$E_{ext}(v_i) = -(\log(P(\mu_{in}(v_i)|a_l^2)) + \log(P(\mu_{out}(v_i)|a_t^2))), \quad (6)$$

with and $P(\mu_{out}(v_i)|a_t^2)$ the estimated Rayleigh distributions around the point v_i, such that:

$$P(y|a^2) = \frac{y}{a^2}\exp\frac{-y^2}{2a^2}. \quad (7)$$

a_l and a_t are the Rayleigh distribution parameters estimated from the averages of the lumen grayscale μ_l and surrounding tissue μ_t on a representative image of the sequence during the initialization step:

$$a = \mu\sqrt{\frac{2}{\pi}}. \quad (8)$$

The mean gray levels $\mu_{in}(v_i)$ and $\mu_{out}(v_i)$ are calculated from the points located in $\phi_{in}(v_i)$ and $\phi_{out}(v_i)$ windows, respectively.

Fig. 5 illustrates the behavior of the likelihoods and $P(\mu_{out}(v_i)|a_t^2)$ for each point v_i (eq. (6)) for 3 cases. Overall, the sum of all $E_{ext}(v_i)$ is minimized when the contour is right on the luminal border (Fig. 5(c and f)). In comparison, Jourdain et al. [35] used only simple Gaussian distributions with a constant variance set by the user in their external energy term.

2.2.3. Helical snake evolution

In classical snake methods, an initialization close to the contour of the intended object is required. To alleviate this constraint, we propose to choose the direction of the displacement of the point $v_i \in V$ according to two log-likelihood ratios calculated on the two windows $\phi_{in}(v_i)$ and $\phi_{out}(v_i)$:

$$R_{in}(v_i) = \frac{log\,(P(\mu_{in}(v_i)|a_l^2))}{log\,(P(\mu_{in}(v_i)|a_t^2))} \quad (9)$$

$$R_{out}(v_i) = \frac{log\,(P(\mu_{out}(v_i)|a_l^2))}{log\,(P(\mu_{out}(v_i)|a_t^2))} \quad (10)$$

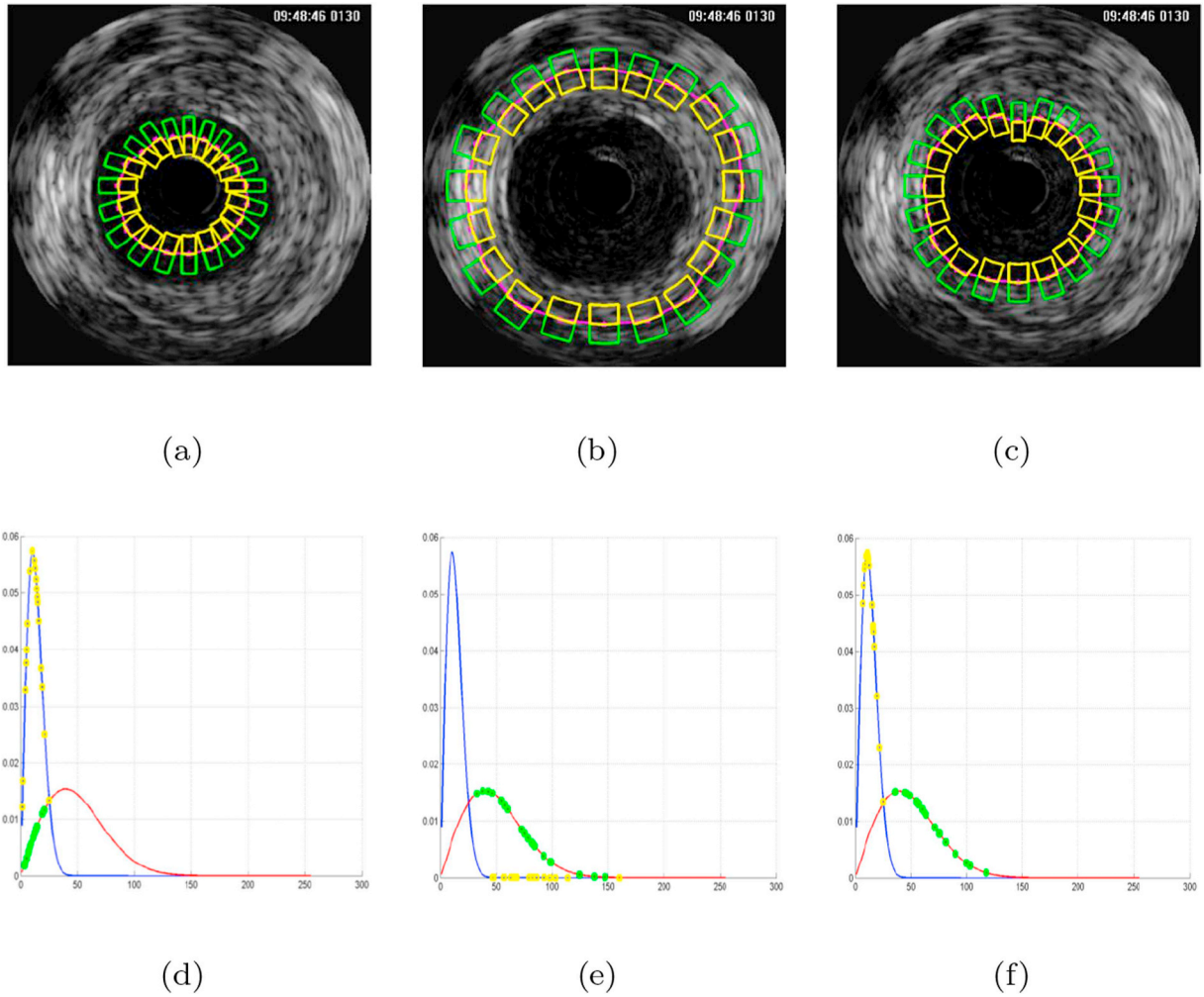

Fig. 5. Three cases for window localization. (a) in the lumen, (b) in the tissue, (c) on the luminal border and (d–f) the distribution of the likelihood of the internal ϕ_{in} (yellow dots) and external ϕ_{out} (green dots) windows for each v_i in the mixtures of lumen and tissue distributions for cases (a–c), respectively.

Algorithm 1 Helical Snake Evolution

```
Initialization of the helical snake;
while not maximal iteration do
    forall helical snake points v_i ∈ V do
        Select φ_in(v_i) and φ_out(v_i);
        Compute μ_in(v_i), μ_out(v_i), R_in(v_i) and R_out(v_i);
        if R_in(v_i) < 1 then
            forall internal neighboring w_j ∈ W_in do
                Select φ_in(w_j) and φ_out(w_j);
                Compute μ_in(w_j), μ_out(w_j), E_int(w_j) and E_ext(w_j);
            end
        elseif R_out(v_i) > 1 then
            forall external neighboring w_j ∈ W_out do
                Select φ_in(w_j) and φ_out(w_j);
                Compute μ_in(w_j), μ_out(w_j), E_int(w_j) and E_ext(w_j);
            end
        end
        Normalization of E_int(w_j) and E_ext(w_j);
        Minimization of E_S(w_j);
        Update the new position of the point v_i;
    end
end
```

when $R_{out}(v_i) > 1$, the point v_i is in the lumen (Fig. 5a) and requires a displacement towards the surrounding tissue (outward) and inversely, when $R_{in}(v_i) < 1$, the point v_i is in the tissue (Fig. 5b) and requires a displacement towards the lumen (inward). Afterwards, the points of the snake are finely moved radially and the new position of the point $v_i \in V$ is chosen as the neighbour $w_j \in W$ that minimizes the energy function.

A normalization procedure adjusts the values of E_{int} and E_{ext}, measured on different scales, to a common scale [0,1] prior to their weighted sum.

Algorithm 1 summarizes all the steps of the proposed helical snake algorithm.

2.3. 3D reconstruction of the lumen

To reconstruct the final volume of the lumen artery, we extract the lumen contour in each frame of the sequence as follows [36]:

- For images which are in the first turn of the helix, the lumen contour is obtained by direct projection of all points constituting the first turn.
- For images lying between two consecutive turns of the helix, the lumen contour is determined by linear interpolation between all points constituting the two consecutive turns [35].
- For images that are in the last turn of the helix, the lumen contour is detected by a direct projection of the points making up the last turn.

Fig. 6, illustrates the steps of 3D reconstruction of the lumen artery.

3. Experimental results

In this section, we present experimental results to provide an insight into the behavior of the 3D helical active contour and demonstrate its interest for IVUS lumen segmentation. The performance of the proposed method was compared with several other IVUS segmentation methods. All programs were implemented using MATLAB R2017a (The MathWorks Inc., Natick, MA, USA) on a computer equipped with Intel (R) core (TM) i7-4500U CPU (1.80 GHz) and 16.0 GB of RAM memory.

3.1. Datasets and parameter setting

The evaluation of our algorithm was performed on two different datasets extracted from in vivo pullbacks of human femoral and coronary arteries with a 20 MHz probe. The sequences had different lengths (150–1200 frames), and the size of the images was 10 mm × 10 mm with a resolution of 384 × 384 pixels. The pixel size was 26 μm× 26 μm. All data were stored in the DICOM format.

The femoral dataset consisted of nine IVUS sequences acquired with Jomed equipment (In-vision gold, Helsingborg, Sweden). The acquisition frequency was 10 images/sec for a catheter pullback velocity set to 1 mm/s [17,35]. The sequences were acquired during an examination of the superficial femoral arteries of either one or both legs of seven patients before undergoing balloon angioplasty. In all cases, the disease was advanced, and the sequences showed severe stenosis (mean plaque burden of 0.46 ± 0.13 with 35% of plaque burden > 50%), bifurcation, calcification, ring-down, and guide wire artifacts. This database derived from a sub-study of a randomized clinical trial published in Ref. [41] in which the details of inclusion and exclusion criteria of patients and lesions are described. A total of 654 images were obtained with ground truth manually segmented by one experimented expert from an accredited IVUS core laboratory at the Montreal Heart Institute.

The coronary dataset was a publicly available dataset described in Ref. [42]. It consisted of 10 IVUS sequences acquired on 10 patients using the Si5 imaging system (Volcano Corporation, California, USA) equipped with a 20 MHz Eagle Eye monorail catheter. A total of 435 images with ground truth were provided. All images contained a plaque (mean plaque burden of 0.43 ± 0.09 with 22% of plaque burden > 50%) and were categorized as follows: 225 images without any serious artifacts, 60 images with bifurcations, 94 images with a side vessel, and 106 images with a shadow artifact. Among these images, 44 contained more than one artifact.

The proposed IVUS lumen segmentation was dependent on the number of points for each turn, the number of turns of the helix, the number of neighbors in W_{in} and W_{out}, the cubic window dimensions of ϕ_{in} and ϕ_{out} (length, width and depth), the weighting parameter α, and the maximum number of iterations. The number of points in each turn of the helical snake was fixed to 35 points. The number of turns of the helix model varied between one and six turns every 10 frames (see Section 3.3). The length of the windows, ϕ_{in} and ϕ_{out}, was initialized at 20 pixels and decreased to 10 pixels as the number of iterations increased. Similarly, the depth of the windows decreased from seven to three images, while the width was adapted automatically according to the distance between two consecutive points (Fig. 3b). This procedure refined the contour detection locally as the helix approached the lumen border. The number of neighbors, w_j, was set to $W_{in} = 3$ and $W_{out} = 3$. The weighting parameter, α, was determined empirically and fixed to 0.65, and the maximum number of iterations was set to 45 for femoral arteries and 35 for coronary arteries[2].

3.2. Evaluation criteria

The assessement of the IVUS segmentation algorithms was based on several evaluation criteria: Average Distance (*AD*), Hausdorff Distance (*HD*) [43,44], Percentage of Area Difference (*PAD*) [42], Dice index (*DC*) [45], Jaccard index (*JM*) [46], sensitivity, specificity, and accuracy [47]. These criteria evaluated the error measurements between the manual contour (ground truth) and the contour obtained by a segmentation method. The evaluation was carried out on the set of 2D images of a sequence for the 2D performance, and on the whole volume of the lumen in voxels for the 3D performance.

Let $C_a = \{a_1, a_2, a_3, ..., a_m\}$ be the set of m points of the lumen contour detected by a segmentation algorithm and let $C_b = \{b_1, b_2, b_3, ..., b_n\}$ be

[2] We found empirically that no improvement occurred with more iterations.

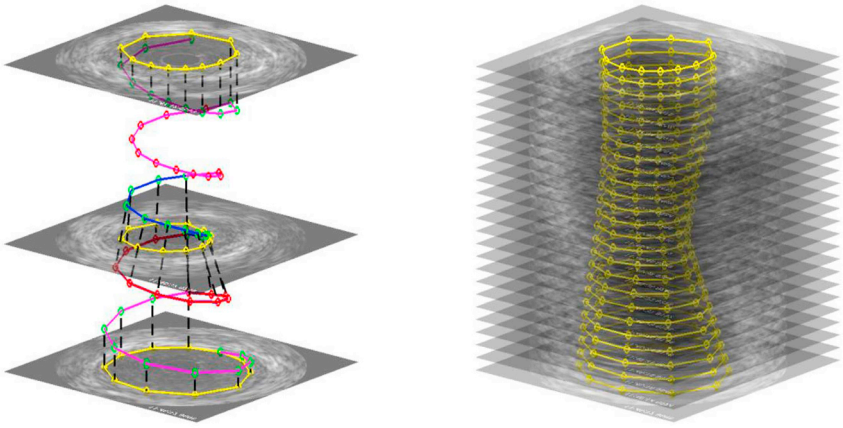

(a) (b)

Fig. 6. 3D Reconstruction of the lumen artery. (a) Computation of 2D contours by interpolation between 2 consecutive turns of helix and direct projection for the first and last turn of the helix, (b) Final 3D Reconstruction.

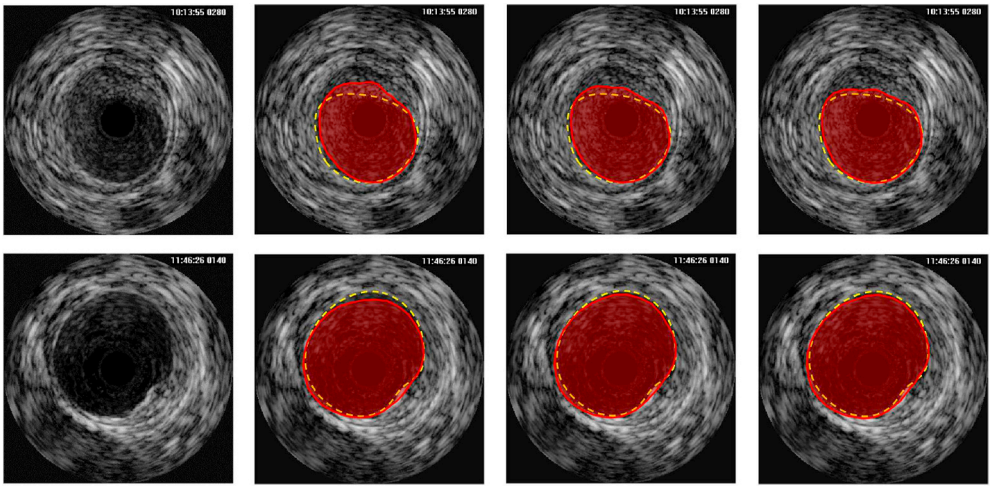

Fig. 7. Influence of the number of helix turns on the segmentation results of femoral arteries. First column: Two IVUS cross-sectional images. Second, third and fourth columns: Detected lumen contours by the helical snake algorithm in red and the ground truth in dotted yellow, with 1, 2 and 3 turns every ten frames, respectively.

Table 1
Evaluation criteria (mean ± standard deviation) and computation time per frame (*CTF*) for different number of helix turns.

Dataset	Turns Number	*AD*	*HD*	*JM*	*DC*	*PAD*	*CTF*
	every ten frames	(mm)	(mm)	(%)	(%)	(%)	(s)
Femoral	1 Turn	0.129 ± 0.065	0.331 ± 0.175	88.80 ± 6.76	93.92 ± 4.17	7.18 ± 10.42	0.05
	2 Turns	0.117 ± 0.060	0.318 ± 0.174	89.92 ± 6.02	94.58 ± 3.63	6.36 ± 8.27	0.10
	3 Turns	0.114 ± 0.061	0.315 ± 0.182	90.15 ± 6.13	94.70 ± 3.76	6.31 ± 9.04	0.15
Coronary	1 Turn	0.147 ± 0.060	0.363 ± 0.155	83.74 ± 6.50	91.01 ± 4.03	7.94 ± 8.62	0.04
	3 Turns	0.110 ± 0.047	0.285 ± 0.141	87.79 ± 5.44	93.40 ± 3.22	5.64 ± 6.49	0.09
	6 Turns	0.103 ± 0.046	0.272 ± 0.138	88.59 ± 5.06	93.87 ± 2.94	5.39 ± 5.53	0.17

Table 2
Improvement of segmentation results between 1 and 3 helix turns every ten frames in stenosis of the femoral dataset.

Sequence	Stenosis (Frame #)	Δ*AD*(mm)	Δ*HD*(mm)	Δ*JM*(%)	Δ*DC*(%)	Δ*PAD*(%)
1	170–330	0.024	0.048	1.94	1.12	0.95
5	280–480	0.035	0.059	3.58	2.11	3.08
6	430–660	0.019	0.059	1.82	1.00	0.62
7	390–540	0.045	0.059	4.90	2.95	7.44

the set of n points of the ground truth. a_i and b_j are represented by their Cartesian coordinates $a_i(x_{ai}, y_{ai})$ and $b_i(x_{bi}, y_{bi})$. We note by A_a and A_b the areas surrounded by the contours C_a and C_b, respectively.

Here are the formulas of each measure.

Average Distance (AD) represents the average of all Euclidean distances between all points that form the algorithm's contour and the ground truth.

$$AD = \frac{1}{min(m,\, n)} \sum_{i=1}^{min(m,n)} \sqrt{(x_{ai} - x_{bi})^2 + (y_{ai} - y_{bi})^2}\ . \tag{11}$$

Hausdorff distance (HD) computes the maximum error distance

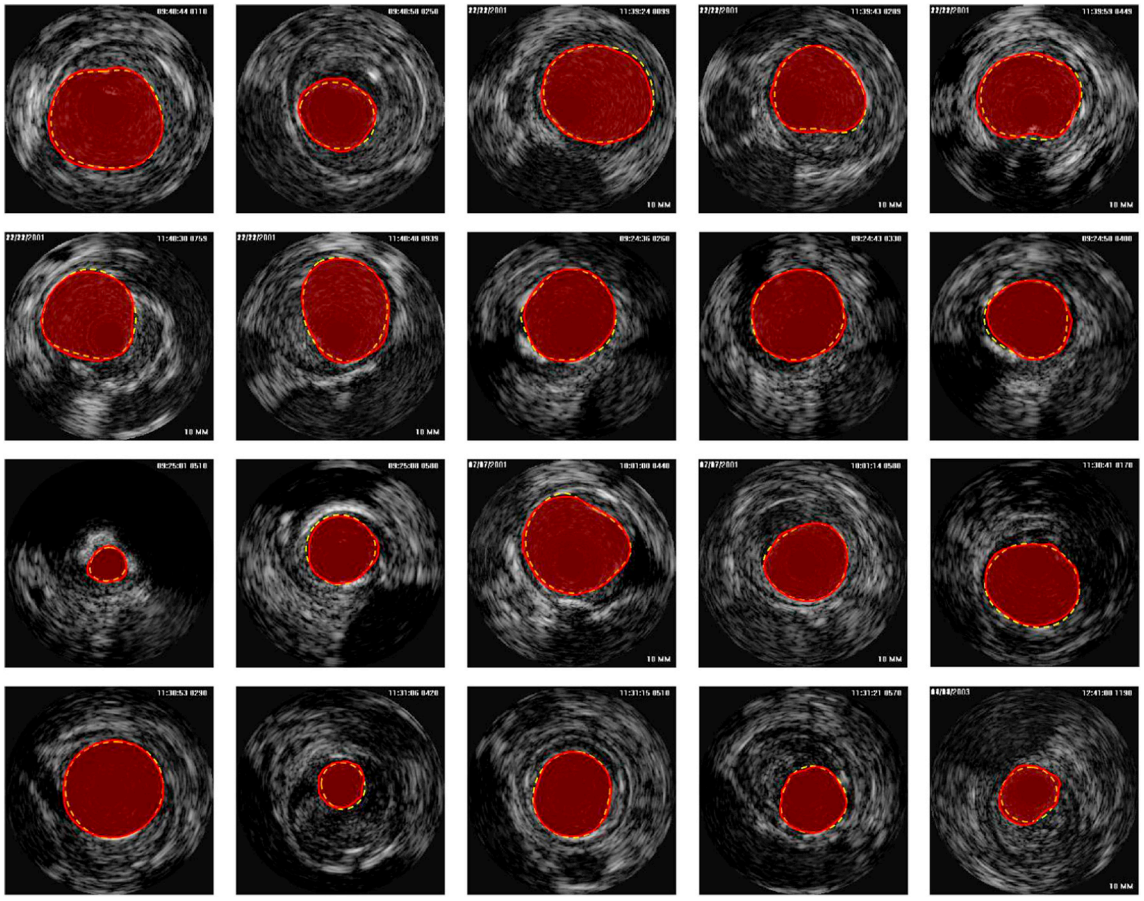

Fig. 8. Results of the helical snake algorithm (red contours) superimposed with the ground truth (yellow dotted contours) on femoral arteries with various difficulties.

between two contours. It is calculated for each 2D frame of each sequence in two steps: For each point a_i, we compute all distances with all the points C_b and we choose the minimum distance:

$$d(a_i, C_b) = \min\|b_j - a_i\|. \tag{12}$$

The same step is applied for all points b_j :

$$d(b_j, C_a) = \min\|a_i - b_j\| . \tag{13}$$

The Hausdorff distance is:

$$HD = max\left(\max_i\{d(a_i, C_b)\}, max_j\{d(b_i, C_a)\}\right). \tag{14}$$

Dice index (DC) is an empirical measure that varies linearly with similarity and describes how one set is similar to another. It is defined as twice the intersection of two areas divided by their sum:

$$DC = \frac{2|A_a \cap A_b|}{|A_a| + |A_b|} . \tag{15}$$

Jaccard index (JM) is a statistical measure that does not vary linearly with similarity. It is defined by the intersection of areas divided by the union of areas:

$$JM = \frac{|A_a \cap A_b|}{|A_a \cup A_b|} . \tag{16}$$

Percentage of Area Difference (PAD) computes the ratio of the difference between the two lumen areas (algorithm and ground truth) to the ground truth area:

$$PAD = \frac{|A_a - A_b|}{A_b} . \tag{17}$$

The sensitivity, specificity and accuracy metrics are determined from the four basic cardinalities of the confusion matrix, which are true positives (TP: number of pixels correctly identified as lumen), false positives (FP: number of pixels incorrectly identified as lumen), true negatives (TN: number of pixels correctly identified as non-lumen), and false negatives (FN: number of lumen pixels misclassified by the method).

Sensitivity represents the ability of the model to correctly identify the lumen pixels:

$$Sensitivity = \frac{TP}{TP + FN} . \tag{18}$$

Specificity defines the ability of the model to correctly identify the non-lumen:

$$Specificity = \frac{TN}{TN + FP} . \tag{19}$$

Accuracy represents the ability of the model to correctly differentiate the lumen and non-lumen pixels:

$$Accuracy = \frac{TP + TN}{TP + TN + FP + FN} . \tag{20}$$

Comparisons of lumen areas with linear regression and Bland–Altman graphs are also provided. Bland–Altman graphs help to visualize potential bias in errors with respect to area detection [33].

3.3. Influence of the number of turns

The reconstruction of the final volume of the artery depends on the spacing between turns. In this section, we show the influence of the

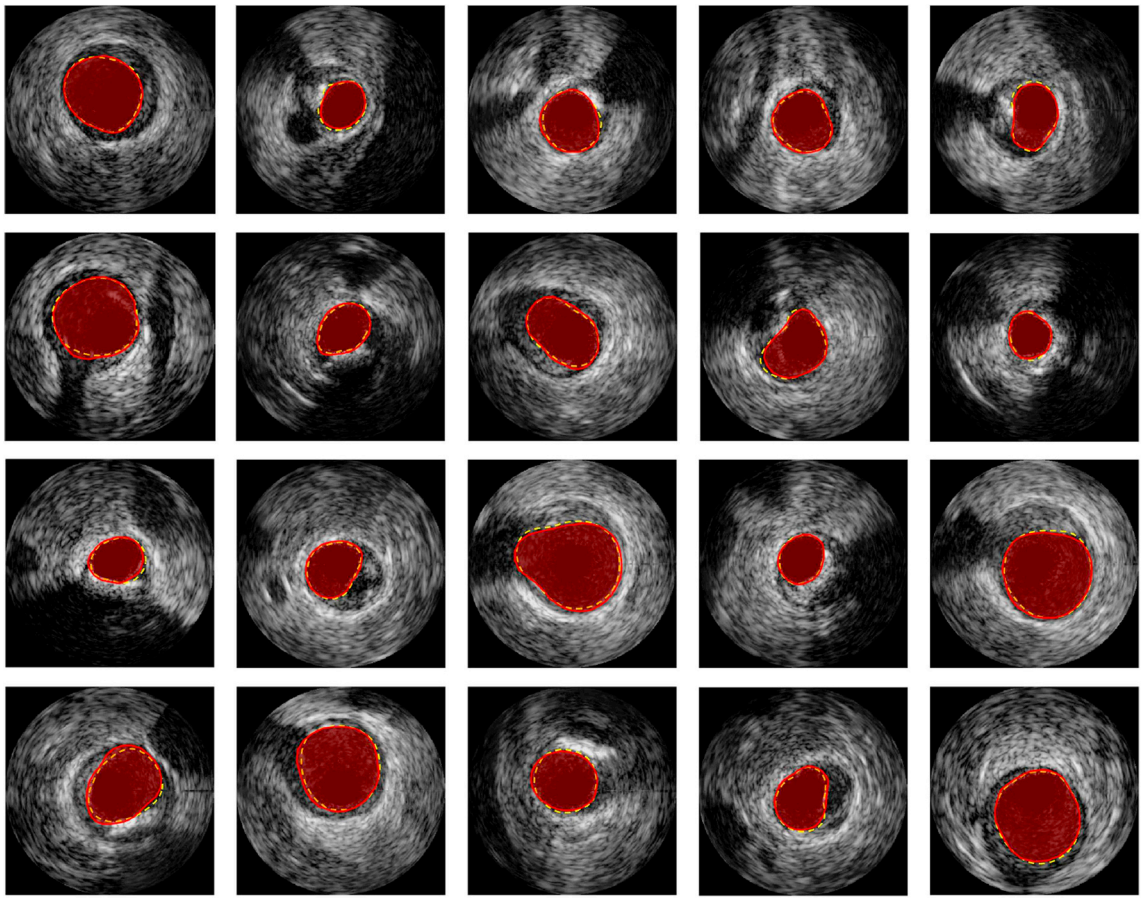

Fig. 9. Results of the helical snake algorithm (red contours) superimposed with the ground truth (yellow dotted contours) on coronary arteries with various difficulties.

number of turns. For this purpose, we performed different measures by varying the number of turns from one to three (every ten frames) on the nine femoral IVUS sequences and from one to six (every ten frames) for the 10 coronary IVUS sequences[3]. Fig. 7 shows the segmentation results (cross-sectional images) on femoral arteries according to the number of turns.

Table 1 displays values of evaluation criteria obtained on all sequences according to the number of turns. Analysis of the qualitative and quantitative results revealed the influence of the number of turns of the helix. For instance, in Fig. 7, we see an improvement in the segmentation results when the number of turns doubles or triples. For the femoral dataset, the overall improvement was 1.35% for the Jaccard measure, 0.015 mm for the average distance, 0.007 mm for the Hausdorff distance and 0.87% for the percentage of area difference when the number of turns was three times higher. For the coronary dataset, the improvement was 4.85% for the Jaccard measure, 0.044 mm for the average distance, 0.091 mm for the Hausdorff distance and 2.55% for the percentage of area difference when the number of turns was six times higher. This improvement was small over the entire sequence, but it was considerable when rapid variations in the lumen volume occurred (e.g., severe stenosis). Table 2 displays the difference in performance between two segmentation results (1 and 3 turns every ten frames) in the presence of severe stenosis (parts of sequences 1, 5, 6 and 7 extracted in femoral arteries). An improvement of 4.90% for the Jaccard index and 2.95% for the Dice index was mainly noted in the seventh sequence. However, this improvement was achieved at the expense of the calculation time which increased with the number of helix turns.

To remedy to this precision/computation-time dilemma, we used a simple strategy that increased the speed of the algorithm without losing accuracy. This strategy involved initializing a helix with a reduced number of turns (one turn every ten frames). Ten iterations before the end of the process, we increased the number of helix turns to three turns for femoral and six turns for coronary (every ten frames) to refine the contour detection locally as the active contour was approaching the lumen border. This procedure reduced the overall computing time approximately by half.

Another possible solution for optimizing the computation time is to increase the number of turns only at the locations of rapid change in the lumen shape (e.g., stenosis) for additional accuracy in these critical regions. Starting with a basic helix with one turn every ten frames, the algorithm could identify the locations of rapid change and then increase the number of turns only in these portions of the sequence for the final iterations.

3.4. Evaluation of the algorithm

We applied the proposed segmentation algorithm on nine femoral IVUS sequences and on 10 coronary IVUS sequences. Figs. 8 and 9 display the segmentation results obtained on some IVUS frames of femoral and coronary datasets, respectively. We can see in both datasets that the detected contours follow correctly the borders of the lumen and often coincide with the ground truth, even in the presence of difficulties like guide wire artifacts, bifurcations, side vessels, stenosis and shadows. Figs. 10 and 11 show that the whole helix obtained by our segmentation method is similar to the ground truth for femoral and

[3] There was no gain with more than 3 turns every 10 frames for femoral arteries and 6 turns every 10 frames for (smaller) coronary arteries.

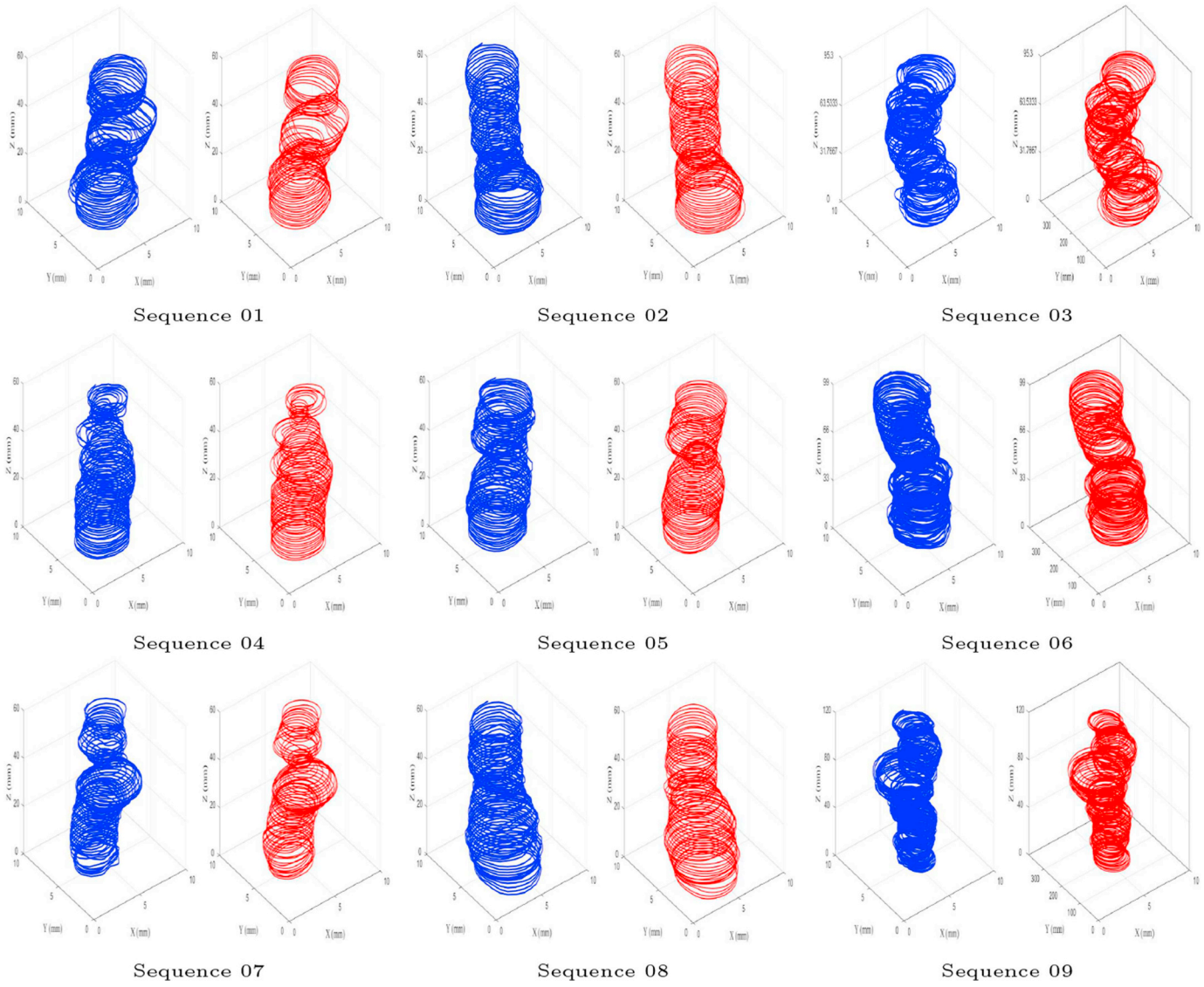

Fig. 10. Helical segmentation results in blue and the ground truth contours in red, for the 9 IVUS femoral sequences.

coronary arteries. In most cases, the algorithm has correctly followed the shape of the lumen. However, some confusion between the boundaries of the media layer and lumen can be observed on some parts of the 3D reconstructions. This was due to the very small thickness and the low brightness of the intima wall (e.g., sequence 6 in Fig. 10).

For a better evaluation of adequacy between the manual and automated segmentations of lumen areas, linear regression analysis and Bland-Altman plots were performed on the IVUS sequences (Fig. 12 for femoral arteries and Fig. 13 for coronary arteries). They indicate both a good agreement with R^2= 0.97 and a slight bias of $-0.27\,mm^2$ and of $0.02\,mm^2$ for femoral and coronary arteries, respectively.

Tables 3 and 4 give the values of the evaluation criteria for each sequence of femoral and coronary datasets, respectively. Overall, the results were very good for both datasets. For the femoral dataset, the second sequence offered the best results with an overlap of 95.91% for the Dice index and 92.21% for the Jaccard index. The best Hausdorff distance was 0.24 mm obtained on the seventh sequence, while the eighth sequence provided the poorest performance with 0.431 mm. For the coronary dataset, the best performance was obtained on the ninth sequence with a Dice index of 96.11% and a Hausdorff distance of 0.090 mm, while the eighth sequence gave the poorest results with 81.62% for the Jaccard measure and 0.472 mm for the Hausdorff distance. These variations were due to the presence of different types of artifact and contrast/brightness.

Table 5 displays the average 2D performance, compared to the inter-observer variability[4]. The values obtained with the algorithm were close to the inter-observer variability for the femoral dataset and lower for the coronary dataset. This is important because it shows that our segmentation errors were comparable or smaller than the typical differences between manual contours traced by two experts, thus confirming the quality of our results. The results also showed the efficiency of our method for the segmentation of IVUS images with an accuracy higher than 98.5%. Table 6 displays the average 3D performance that shared approximatively the same values as the 2D assessment.

3.5. Comparison with other methods

A quantitative comparison with other methods using a similar 20–30 MHz transducer, was performed in order to validate the performance of our IVUS lumen segmentation method. Table 7 gives some details about these methods. Table 8 displays the evaluation criteria (mean ± standard deviation) organized according to the type of artery

[4] Computed with contours manually traced by a second expert [18, 42].

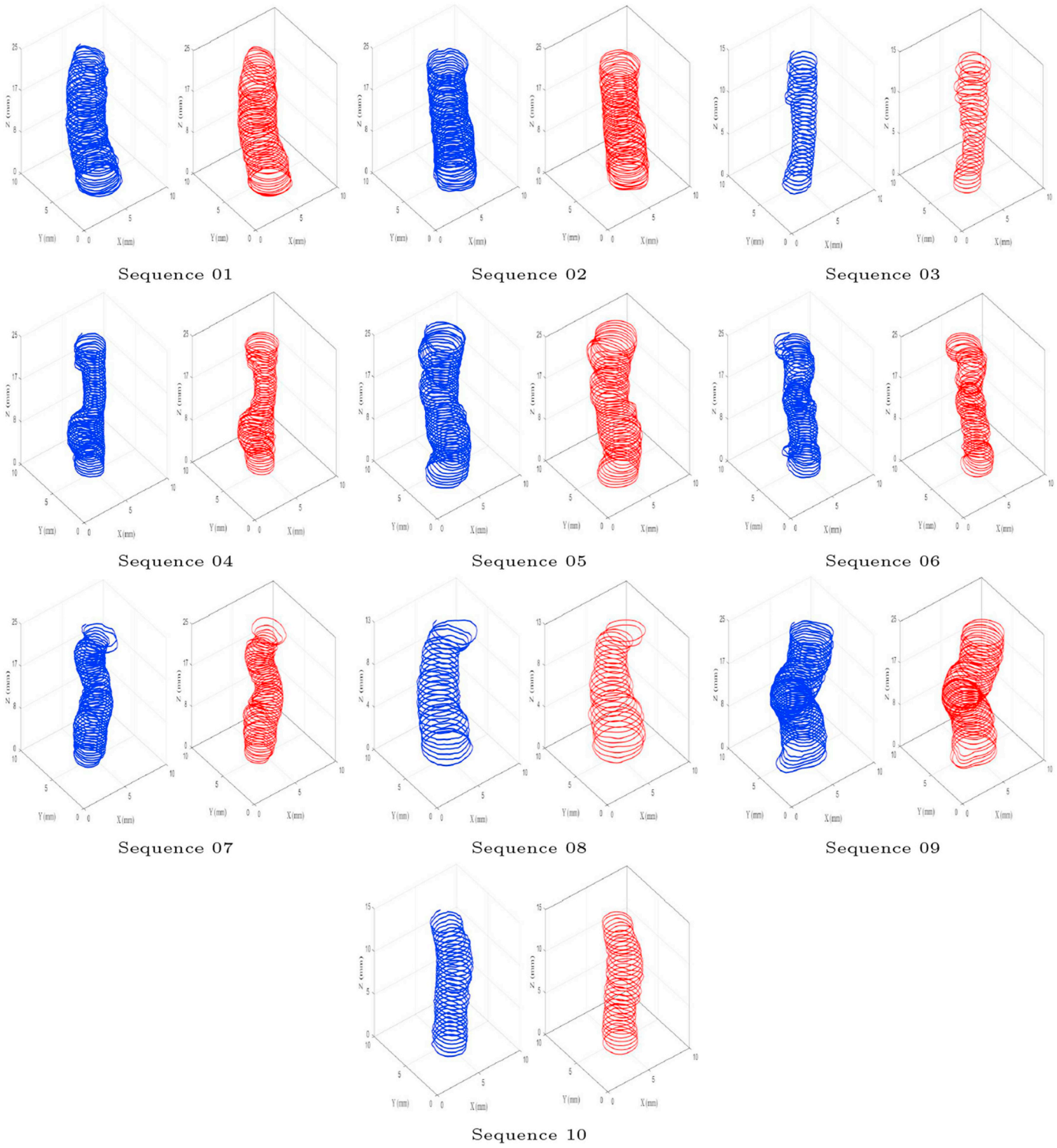

Fig. 11. Helical segmentation results in blue and the ground truth contours in red, for the 10 IVUS coronary sequences.

(femoral or coronary). Table 9 displays a comparison with methods which used the same coronary dataset [42], for various categories. The best results are highlighted in bold.

Different datasets, data dimension (2D/3D), artery type and manual or automatic initialization make comparison difficult in Table 8. However, in a general way, our method provided very satisfying results.

First, our method outperformed the methods in Refs. [17,35] that used the same femoral dataset. Indeed, the improvement against [35] was 0.13 mm for average distance and 0.30 mm for Hausdorff distance. Recall that [35] used a basic helical snake and required an initial contour close to the lumen borders. Our method was also better in term of accuracy than more complex methods using 3D meshes and propagation surfaces with manual initialization [17,18]. The comparison with 3D methods [17,18,35] showed the superiority of the proposed method.

For coronary arteries, our method also outperformed all others

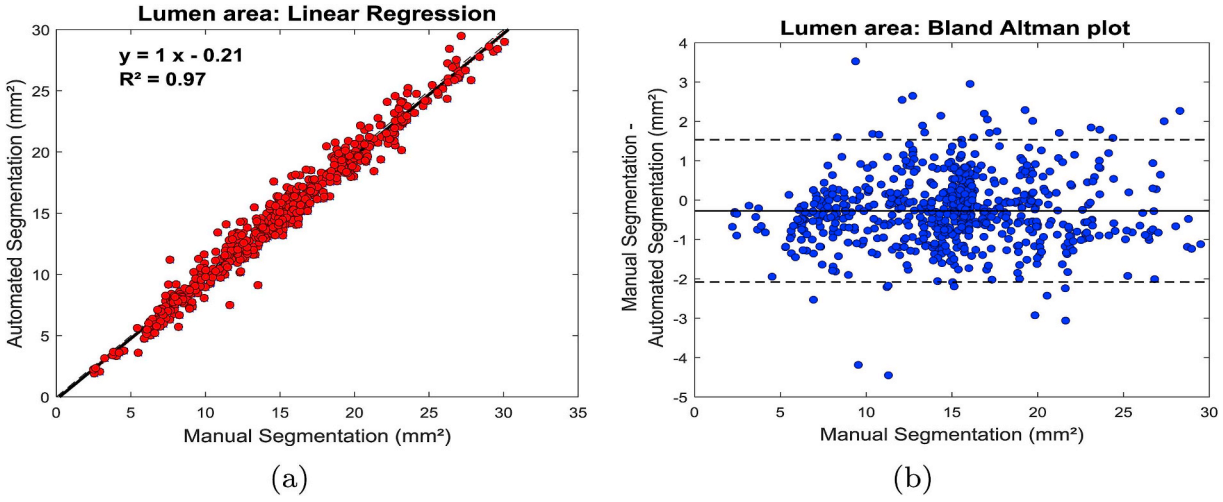

Fig. 12. Comparison of the femoral lumen areas between algorithm and ground truth. (a) Linear Regression. (b) Bland-Altman plot.

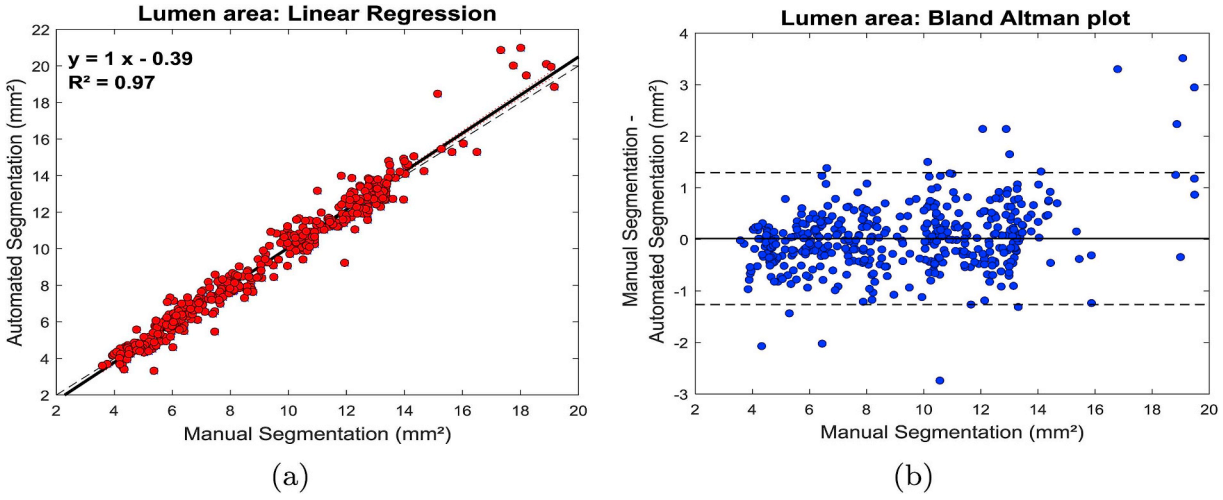

Fig. 13. Comparison of the coronary lumen areas between algorithm and ground truth. (a) Linear Regression. (b) Bland-Altman plot.

Table 3
Evaluation criteria (mean ± standard deviation) for each femoral sequence.

Sequence	Plaque Burden (%)	*AD*(mm)	*HD*(mm)	*JM*(%)	*DC*(%)	*PAD*(%)
1	49.67 ± 11.13	0.135 ± 0.061	0.368 ± 0.153	89.64 ± 4.11	94.50 ± 2.32	3.84 ± 2.72
2	42.01 ± 10.46	0.106 ± 0.047	0.279 ± 0.138	92.21 ± 3.64	95.91 ± 2.00	6.26 ± 4.81
3	48.58 ± 8.29	0.122 ± 0.058	0.354 ± 0.187	90.04 ± 4.59	94.69 ± 2.62	4.50 ± 3.62
4	44.27 ± 11.59	0.100 ± 0.049	0.317 ± 0.171	89.43 ± 7.50	94.24 ± 4.55	7.38 ± 10.94
5	41.85 ± 16.40	0.118 ± 0.076	0.309 ± 0.187	90.43 ± 6.67	94.84 ± 3.99	9.53 ± 9.95
6	33.40 ± 8.44	0.108 ± 0.055	0.284 ± 0.133	91.89 ± 3.89	95.73 ± 2.17	3.10 ± 5.34
7	55.29 ± 12.29	0.089 ± 0.048	0.241 ± 0.145	91.09 ± 5.97	95.23 ± 3.51	5.34 ± 5.58
8	37.71 ± 12.34	0.155 ± 0.067	0.431 ± 0.206	88.91 ± 5.54	94.03 ± 3.26	5.87 ± 4.27
9	53.77 ± 9.73	0.100 ± 0.043	0.264 ± 0.104	89.21 ± 5.19	94.21 ± 3.03	7.49 ± 7.03
All Frames	45.55 ± 13.14	0.113 ± 0.058	0.311 ± 0.165	90.29 ± 5.36	94.81 ± 3.13	5.89 ± 6.48

methods using the same dataset [42], except the methods reported in Refs. [12,27] for *AD* and *HD*, and [22] for *HD* and *JM*. This can be explained by the fact that these methods were applied on another dataset. It is also important to note that these methods run only on 2D images and the number of tested frames was small in Ref. [12]. In Refs. [22,27], the selected subjects contained only moderate or mild atherosclerosis, without bifurcation, dense calcifications, or other complex lesions. However, our method gave better results than the more complex method using 3D contour, developed in Ref. [42]. Table 9 shows that our algorithm performs well in all vessels with various morphological characteristics.

Table 7 also displays the computation times obtained by our method and those reported in the literature. Although the running times are computer dependent, they gave an idea of the computation time required by the algorithms according to artery type (femoral/coronary), the dimension of contours (2D/3D) and the number of segmented regions (lumen alone or with media). Our method appeared faster than other techniques working under the same conditions.

Table 4
Evaluation criteria (mean ± standard deviation) for each coronary sequence.

Sequence	Plaque Burden (%)	*AD*(mm)	*HD*(mm)	*JM*(%)	*DC*(%)	*PAD*(%)
1	40.52 ± 7.70	0.124 ± 0.032	0.304 ± 0.132	88.06 ± 3.23	93.62 ± 1.85	4.25 ± 4.25
2	37.39 ± 5.51	0.093 ± 0.025	0.272 ± 0.114	91.26 ± 2.58	95.41 ± 1.42	3.92 ± 3.05
3	44.32 ± 4.48	0.115 ± 0.037	0.300 ± 0.089	83.83 ± 5.68	91.10 ± 3.40	5.28 ± 3.52
4	43.31 ± 7.62	0.082 ± 0.018	0.229 ± 0.081	88.87 ± 3.23	94.08 ± 1.83	3.61 ± 2.37
5	41.69 ± 7.77	0.079 ± 0.033	0.247 ± 0.178	91.86 ± 3.71	95.72 ± 2.08	4.52 ± 3.32
6	52.52 ± 9.02	0.102 ± 0.041	0.284 ± 0.160	86.32 ± 5.40	92.57 ± 3.18	8.89 ± 7.52
7	44.52 ± 12.71	0.093 ± 0.044	0.262 ± 0.151	87.45 ± 6.11	93.18 ± 3.73	7.43 ± 10.30
8	43.69 ± 9.33	0.207 ± 0.060	0.472 ± 0.161	81.62 ± 3.70	89.84 ± 2.26	8.37 ± 7.33
9	39.95 ± 4.83	0.090 ± 0.025	0.227 ± 0.082	92.53 ± 2.27	96.11 ± 1.24	3.62 ± 2.34
10	37.73 ± 7.64	0.110 ± 0.044	0.250 ± 0.072	88.16 ± 4.32	93.65 ± 2.47	5.34 ± 4.09
All Frames	42.63 ± 0.04	0.104 ± 0.046	0.275 ± 0.139	88.55 ± 5.09	93.85 ± 2.97	5.38 ± 5.68

Table 5
Average 2D performance.

		AD (mm)	*HD* (mm)	*JM* (%)	*DC* (%)	*PAD* (%)	*Sensitivity* (%)	*Specificity* (%)	*Accuracy* (%)
Femoral	Our method	0.11 ± 0.06	0.31 ± 0.16	90.29 ± 5.36	94.81 ± 3.13	5.89 ± 6.48	96.15 ± 3.93	99.01 ± 0.66	98.59 ± 0.78
	Inter-observer	0.10 ± 0.04	0.25 ± 0.09	91.31 ± 4.32	95.40 ± 2.46	6.69 ± 5.29	92.81 ± 4.17	99.78 ± 0.20	98.83 ± 0.46
Coronary	Our method	0.10 ± 0.05	0.27 ± 0.14	88.55 ± 5.09	93.85 ± 2.97	5.38 ± 5.68	94.26 ± 4.37	99.42 ± 0.38	98.94 ± 0.64
	Inter-observer	0.11 ± 0.04	0.28 ± 0.13	87.97 ± 5.10	93.52 ± 3.00	10.70 ± 7.89	98.13 ± 2.63	99.08 ± 0.54	99.02 ± 0.45

Table 6
Average 3D performance.

		JM (%)	*DC* (%)	*PAD* (%)	*Sensitivity* (%)	*Specificity* (%)	*Accuracy* (%)
Femoral	Proposed method	90.97 ± 1.17	95.27 ± 0.64	5.03 ± 1.42	96.07 ± 1.73	98.87 ± 0.44	98.54 ± 0.41
	Inter-observer	92.22 ± 1.69	95.95 ± 0.92	5.93 ± 1.18	93.40 ± 1.18	99.79 ± 0.07	98.83 ± 0.21
Coronary	Proposed method	88.00 ± 3.48	93.59 ± 1.99	5.34 ± 1.82	93.58 ± 2.40	99.39 ± 0.26	98.86 ± 0.57
	Inter-observer	88.45 ± 2.86	93.85 ± 1.63	9.65 ± 4.12	98.01 ± 1.11	99.12 ± 0.31	99.05 ± 0.24

Table 7
Details about our method and others reported in the literature.

Authors	2D/3D	Initial contour	Category	Frames	Artery type	Hardware used	Time per frame
Faraji et al. [29]	2D	Auto	Lumen and media	435	Coronary	Core i7-4700HQ 2.4 GHz	0.16 s
Jodas et al. [28]	2D	Auto	Lumen	326	Coronary	Core i7-4700HQ 2.4 GHz	5.72 ± 1.54 s
Su et al. [22]	2D	Auto	Lumen and media	461	Coronary	Xeon E5-2650 2.0 GHz	–
Lo Vercio et al. [24]	2D	Auto	Lumen	149	Coronary	Core i7-3630QM 2.4 GHz	[1.27 4.59] s
Gao et al. [27]	2D	Auto	Lumen and media	337	Coronary	Pentium Dual-Core 3.19 GHz	16.39 ± 9.62 s
Destrempes et al. [13]	2D	Manual	Lumen and media	435	Coronary	Core i7- Q740 @ 1.73 GHz	8.64 s
Mendizabel et al. [23]	2D	Manual	Lumen	435	Coronary	Core i7 2 GHz	4.96 s
Alberti et al. [42]	3D	Manual	Lumen	435	Coronary	Core 2, Duo 2.13 GHz	13 s
Vard et al. [12]	2D	Auto	Lumen and media	40	Coronary	–	–
Roy-Cardinal et al. [18]	3D	Manual	Lumen and media	440	Femoral	AMD Athlon 64 2 GHz	1.7± 0.3 s
Jourdain et al. [35]	3D	Manual	Lumen	540	Femoral	–	–
Taki et al. [10]	2D	Auto	Lumen and media	420	Coronary	–	–
Unal et al. [19]	2D	Auto	Lumen and media	435	Coronary	Pentium 6200 2.13 GHz	3.25 s
Downe et al. [8]	3D	Auto	Lumen and media	435	Coronary	Core 2 2.4 GHz	0.16 s
Roy-Cardinal et al. [17]	3D	Manual	Lumen and media	540	Femoral	Pentium IV 2.6 GHz	≃ 1 s
Our method	3D	Auto	Lumen	435	Coronary	Core i7-4500U 1.8 GHz	0.07 s
	3D	Auto	Lumen	654	Femoral	Core i7-4500U 1.8 GHz	0.07 s

Finally, we can conclude that overall, our method was competitive with the top segmentation algorithms with the important advantages of a simple implementation, easy initialization and best computing time with 0.07 s per frame. The reported computing time was obtained with MATLAB code without any optimization or GPU acceleration and consequently our method could be implemented for real-time monitoring with these enhancements.

In this paper, the Rayleigh distribution parameters of the lumen and the tissue were estimated in the initialization step on a representative image of the sequence. However, improvements in segmentation results could be obtained by re-estimating these parameters at evenly-spaced intervals in the sequence and updating them at each iteration. This technique would not significantly increase the computing time for large intervals (e.g., 50 or more frames).

4. Conclusion

In this research, we proposed a 3D helix snake segmentation technique for the identification of the blood vessel lumen using IVUS imaging. Experimental results for several IVUS sequences acquired in large-diameter arteries (femoral arteries) and small-diameter arteries (coronary arteries) typically affected by different artifacts showed the

Table 8
Errors and overlap (mean ± standard deviation) for other works reported in literature.

Dataset	Authors	Remark	*AD* (mm)	*HD* (mm)	*JM*	*DC*	*PAD*
Femoral	Roy-Cardinal et al., 2010 [18]		0.13 ± 0.10	0.43 ± 0.30	–	–	–
	Jourdain et al., 2010 [35]		0.24 ± 0.14	0.61 ± 0.30	–	–	–
	Roy-Cardinal et al., 2006 [17]	PDFs	0.16 ± 0.10	0.40 ± 0.25	–	–	–
		Gradient	0.14 ± 0.10	0.39 ± 0.24	–	–	–
	Our method		**0.11 ± 0.06**	**0.31 ± 0.16**	**0.90 ± 0.05**	**0.95 ± 0.03**	**0.06 ± 0.06**
Coronary	Faraji et al., 2018 [29]	(⋆)	–	0.30 ± 0.20	0.87 ± 0.06	–	0.08 ± 0.09
	Jodas et al., 2017 [28]	Without C-E (⋆)	–	0.30 ± 0.18	0.87 ± 0.07	0.93 ± 0.04	0.09 ± 0.08
		With C-E (⋆)	–	0.29 ± 0.17	0.88 ± 0.06	0.94 ± 0.04	0.09 ± 0.07
	Su et al., 2017 [22]		–	**0.224**	**0.918**	–	–
	Lo Vercio et al., 2016 [24]	(⋆)	–	–	0.83 ± 0.05	–	0.18 ± 0.06
	Gao et al., 2015 [27]		0.08 ± 0.04	0.24 ± 0.12	–	–	–
	Destrempes et al., 2014 [13]	(⋆⋆)	–	0.34 ± 0.14	0.88 ± 0.05	–	0.06 ± 0.05
	Mendizabel et al., 2013 [23]	(⋆⋆)	–	0.38 ± 0.26	0.84 ± 0.08	–	0.11 ± 0.11
	Alberti et al., 2014 [42]	(⋆⋆)	–	0.46 ± 0.30	0.79 ± 0.08	–	0.16 ± 0.09
	Vard et al., 2012 [12]		**0.07 ± 0.05**	0.30 ± 0.19	–	–	–
	Taki et al., 2008 [10]	Parametric	0.30 ± 0.25	0.88 ± 0.31	–	–	–
		Geometric	0.20 ± 0.15	0.71 ± 0.25	–	–	–
	Unal et al., 2008 [19]	(⋆⋆)	–	0.47 ± 0.39	0.81 ± 0.12	–	0.14 ± 0.13
	Downe et al., 2008 [8]	(⋆⋆)	–	0.47 ± 0.22	0.77 ± 0.09	–	0.15 ± 0.12
	Our method	(⋆)	0.10 ± 0.05	0.27 ± 0.14	0.89 ± 0.05	**0.94 ± 0.03**	**0.05 ± 0.06**

(⋆⋆) Result and data from Balocco et al. [42], (⋆) Data from Balocco et al. [42]. (C-E) Contrast Enhancement,(PDF) Probability Density Function.

Table 9
Errors and overlap (mean ± standard deviation) evaluated on 435 frames of coronary dataset (B) [42] and categorized according to the morphological characteristics of each frame.

	Authors	*HD* (mm)	*JM*	*PAD*
No Artifact	Proposed method	**0.26 ± 0.11**	**0.90 ± 0.04**	**0.05 ± 0.04**
	Faraji et al. [29]	0.29 ± 0.17	0.88 ± 0.05	0.08 ± 0.07
	Lo Vercio et al. [24]	–	0.83 ± 0.05	0.18 ± 0.06
Bifurcation	Proposed method	**0.40 ± 0.21**	**0.85**± 0.07	**0.08**± 0.10
	Faraji et al. [29]	0.53 ± 0.34	0.79 ± 0.10	0.15 ± 0.17
	Destrempes et al. [13]	0.42 ± 0.18	**0.85 ± 0.06**	**0.08 ± 0.06**
	Downe et al. [8]	0.64 ± 0.27	0.70 ± 0.11	0.21 ± 0.15
	Alberti et al. [42]	0.61 ± 0.43	0.75 ± 0.10	0.20 ± 0.10
Side Vessels	Proposed method	0.25 ± 0.12	**0.88 ± 0.05**	**0.05 ± 0.04**
	Faraji et al. [29]	**0.24 ± 0.11**	0.87 ± 0.05	0.06 ± 0.05
	Destrempes et al. [13]	0.36 ± 0.15	0.87 ± 0.04	0.07 ± 0.04
	Downe et al. [8]	0.46 ± 0.19	0.77 ± 0.08	0.15 ± 0.11
	Alberti et al. [42]	0.47 ± 0.24	0.79 ± 0.07	0.17 ± 0.09
Shadow	Proposed method	**0.28 ± 0.13**	0.86 ± 0.07	**0.06**± 0.06
	Faraji et al. [29]	0.29 ± 0.20	0.86 ± 0.07	0.08 ± 0.09
	Destrempes et al. [13]	0.39 ± 0.18	**0.87 ± 0.05**	**0.06 ± 0.05**
	Downe et al. [8]	0.55 ± 0.26	0.76 ± 0.11	0.14 ± 0.13
	Alberti et al. [42]	0.53 ± 0.29	0.78 ± 0.08	0.18 ± 0.09

efficacy of the proposed method. The performance matched or outperformed the best segmentation algorithms that have been reported in the literature. In addition to a high level of accuracy, the main advantages of this method are its simplicity (an evolving curve instead of surface), fast computation time, and no need for initialization of the snake close to the contour to be segmented (lumen).

The helical model can also be adapted for the segmentation of the media-adventitia with another set of parameters. Preliminary tests yielded good results on easy IVUS sequences, but more work is needed for sequences that contain difficulties (such as a shadow, bifurcation, or a side vessel). We plan to investigate the simultaneous segmentation of lumen and media in our future work. Adding another helix to segment the media would only slightly increase the processing time with an independent parallel implementation (e.g., with two or more processors) with some interactions between both contours.

Thanks to its speed, the helix model we have developed can easily be adapted with code optimization to display real-time segmentation for the benefit of the clinician.

Acknowledgments

The authors would like to thank the NSERC for supporting this work.

References

[1] World Health Organization, Cardiovascular diseases (cvds), (1948) http://www.who.int/news-room/fact-sheets/detail/cardiovascular-diseases-(cvds) , Accessed date: 16 November 2018.
[2] M. Sonka, X. Zhang, M. Siebes, M.S. Bissing, S.C. DeJong, S.M. Collins, C.R. McKay, Segmentation of intravascular ultrasound images:a knowledge-based approach, IEEE Trans.on Medical Imaging 14 (4) (1995) 719–732, https://doi.org/10.1109/42.476113.
[3] X. Zhang, C.R. McKay, M. Sonka, Tissue characterization in intravascular ultrasound images, IEEE Trans.on Medical Imaging 17 (6) (1998) 889–899, https://doi.org/10.1109/42.746622.
[4] A. Takagi, K. Hibi, X. Zhang, T.J. Teo, H.N. Bonneau, P.G. Yock, P.J. Fitzgerald, Automated contour detection for high-frequency intravascular ultrasound imaging: a technique with blood noise reduction for edge enhancement, Ultrasound Med. Biol. 26 (6) (2000) 1033–1041, https://doi.org/10.1016/S0301-5629(00)00251-9.
[5] J.-L. Jones, X. Xie, E. Essa, Segmentation of intravascular ultrasound images using graph search and a novel cost function) with the title(Combining region-based and imprecise boundary-based cues for interactive medical image segmentation, Int. J. Numer. Meth. Biomed. Eng. 30 (12) (2014) 1649–1666, https://doi.org/10.1002/cnm.2693.
[6] K. Li, X. Wu, D.Z. Chen, M. Sonka, Optimal surface segmentation in volumetric images a graph-theoretic approach, IEEE Trans. Pattern Anal. Mach. Intell. 28 (1) (2006) 119–134, https://doi.org/10.1109/TPAMI.2006.19.
[7] A. Wahle, J.J. Lopez, M.E. Olszewski, S.C. Vigmostad, K.B. Chandran, J.D. Rossen, M. Sonka, Plaque development, vessel curvature, and wall shear stress in coronary arteries assessed by x-ray angiography and intravascular ultrasound, Med. Image Anal. 10 (4) (2006) 615–631, https://doi.org/10.1016/j.media.2006.03.002.
[8] R. Downe, A. Wahle, T. Kovarnik, H. Skalicka, J. Lopez, J. Horak, M. Sonka, Segmentation of intravascular ultrasound images using graph search and a novel cost function, 2nd workshop on computer vision for intravascular and intracardiac imaging, MICCAI-CVII 2008, 2008, pp. 71–79.
[9] S. Sun, M. Sonka, R.R. Beichel, Graph-based IVUS segmentation with efficient computer-aided refinement, IEEE Trans. Med. Imag. 32 (8) (2013) 1536–1549, https://doi.org/10.1109/TMI.2013.2260763.
[10] A. Taki, Z. Najafi, A. Roodaki, S.K. Setarehdan, R.A. Zoroofi, A. Konig, N. Navab, Automatic segmentation of calcified plaques and vessel borders in IVUS images, Int J CARS 3 (3-4) (2008) 347–354, https://doi.org/10.1007/s11548-008-0235-4.
[11] X. Zhu, P. Zhang, J. Shao, Y. Cheng, Y. Zhang, J. Bai, A snake-based method for segmentation of intravascular ultrasound images and its in vivo validation, Ultrasonics 51 (2) (2011) 181–189, https://doi.org/10.1016/j.ultras.2010.08.001.
[12] A. Vard, K. Jamshidi, N. Movahhedinia, An automated approach for segmentation of intravascular ultrasound images based on parametric active contour models, Australasian Physical and Engineering Sciencees in Medicine 35 (2) (2012) 135–150, https://doi.org/10.1007/s13246-012-0131-7.
[13] F. Destrempes, M.-H.R. Cardinal, L. Allard, J.-C. Tardif, G. Cloutier, Segmentation method of intravascular ultrasound images of human coronary arteries, Comput.

Med. Imag. Graph. 38 (2) (2014) 91–103, https://doi.org/10.1016/j.compmedimag.2013.09.004.
[14] J.D. Klingensmith, R. Shekhar, D.G. Vince, Evaluation of three-dimensional segmentation algorithms for the identification of luminal and medial-adventitial borders in intravascular ultrasound images, IEEE Trans.on Medical Imaging 19 (10) (2000) 996–1011, https://doi.org/10.1109/42.887615.
[15] G. Kovalski, R. Beyar, R. Shofti, H. Azhari, Three-dimensional automatic quantitative analysis of intravascular ultrasound images, Ultrasound Med. Biol. 26 (4) (2000) 527–537, https://doi.org/10.1016/S0301-5629(99)00167-2.
[16] R.M. Cothren, D.G. Vince, J.D. Thomas, J.F. Cornhill, Three-dimensional segmentation of luminal and adventitial borders in serial intravascular ultrasound images, Comput. Med. Imag. Graph. 23 (6) (1999) 299–309, https://doi.org/10.1016/S0895-6111(99)00029-4.
[17] M.-H.R. Cardinal, J. Meunier, G. Soulez, R.L. Maurice, E. Therasse, G. Cloutier, Intravascular ultrasound image segmentation : A three-dimensional fast-marching method based on gray level distributions, IEEE Trans. Med. Imag. 25 (5) (2006) 590–601, https://doi.org/10.1109/TMI.2006.872142.
[18] M.-H.R. Cardinal, G. Soulez, J-C. Tardif, J. Meunier, G. Cloutier, Fast-marching segmentation of three-dimensional intravascular ultrasound images: A pre- and post-intervention study, Med. Phys. 37 (7) (2010) 3633–3647, https://doi.org/10.1118/1.3438476.
[19] G. Unal, S. Bucher, S. Carlier, G. Slabaugh, T. Fang, K. Tanaka, Shape-driven segmentation of the arterial wall in intravascular ultrasound images, IEEE Trans. Inf. Technol. Biomed. 12 (3) (2008) 335–347, https://doi.org/10.1109/TITB.2008.920620.
[20] E. Bovenkamp, J. Djikstra, J. Bosh, J. Reiber, Multi-agent segmentation of IVUS images, Pattern Recogn. 37 (4) (2004) 647–663, https://doi.org/10.1016/j.patcog.2003.09.015.
[21] M.E. Olszewski, A. Wahle, S.C. Mitchell, M. Sonka, Segmentation of intravascular ultrasound images: a machine learning approach mimicking human vision, Int. Congr. 1268 (2004) 1045–1049, https://doi.org/10.1016/j.ics.2004.03.252.
[22] S. Su, Z. Hu, Q. Lin, W.K. Hau, Z. Gao, H. Zhang, An artificial neural network method for lumen and media-adventitia border detection in IVUS, Comput. Med. Imag. Graph. 57 (2017) 29–39, https://doi.org/10.1016/j.compmedimag.2016.11.003.
[23] E.G. Mendizabal-Ruiz, M. Rivera, I. Kakadiaris, Segmentation of the luminal border in intravascular ultrasound B-mode images using a probabilistic approach, Med. Image Anal. 17 (6) (2013) 649–670, https://doi.org/10.1016/j.media.2013.02.003.
[24] L.Lo Vercio, J.I. Orlando, M. del Fresno, I. Larrabide, Assessment of image features for vessel wall segmentation in intravascular ultrasound images, Int J CARS 11 (8) (2016) 1397–1407, https://doi.org/10.1007/s11548-015-1345-4.
[25] O. Ronneberger, P. Fischer, T. Brox, U-net, Convolutional networks for biomedical image segmentation, in: N. Navab, J. Hornegger, W. William, A. Frangi (Eds.), Medical Image Computing and Computer-Assisted Intervention – MICCAI 2015, Springer International Publishing, Cham, 2015, pp. 234–241, , https://doi.org/10.1007/978-3-319-24574-4_28.
[26] D. Mishra, S. Chaudhury, M. Sarkar, A. S. Soin, Ultrasound image segmentation: A deeply supervised network with attention to boundaries, IEEE (Inst. Electr. Electron. Eng.) Trans. Biomed. Eng. https://doi.org/10.1109/TBME.2018.2877577.
[27] Z. Gao, W.K. Hau, M. Lu, W. Huang, H. Zhang, W. Wu, X. Liu, Y.-T. Zhang, Automated framework for detecting lumen and media-adventitia borders in intravascular ultrasound images, Ultrasound Med. Biol. 41 (7) (2015) 2001–2021, https://doi.org/10.1016/j.ultrasmedbio.2015.03.022.
[28] D.S. Jodas, A.S. Pereira, Jao Manuel, R.S. Tavares, Automatic segmentation of the lumen region in intravascular images of the coronary artery, Med. Image Anal. 40 (2017) 60–79, https://doi.org/10.1016/j.media.2017.06.006.
[29] M. Faraji, I. Cheng, I. Naudin, A. Basu, Segmentation of arterial walls in intravascular ultrasound cross-sectional images using extremal region selection, Ultrasonics 84 (2018) 356–365, https://doi.org/10.1016/j.ultras.2017.11.020.
[30] M.C. Moraes, S.S. Furuie, Automatic coronary wall segmentation in intravascular ultrasound images using binary morphological reconstruction, Ultrasound Med. Biol. 37 (9) (2011) 1486–1499, https://doi.org/10.1016/j.ultrasmedbio.2011.05.018.
[31] C. Haas, H. Ermert, S. Holt, P. Grewe, A. Machraoui, J. Barmeyer, Segmentation of 3d intravascular ultrasonic images based on a random field model, Ultrasound Med. Biol. 26 (2) (2000) 297–306, https://doi.org/10.1016/S0301-5629(99)00139-8.
[32] J.A. Noble, D. Boukerroui, Ultrasound image segmentation: A survey, IEEE Trans. Med. Imag. 25 (8) (2006) 987–1010, https://doi.org/10.1109/TMI.2006.877092.
[33] A. Katouzian, E.D. Angelini, S.G. Carlier, J.S. Suri, N. Navab, A.F. Laine, A state-of-the-art review on segmentation algorithms in intravascular ultrasound (IVUS) images, IEEE Trans. Inf. Technol. Biomed. 16 (5) (2012) 823–834, https://doi.org/10.1109/TITB.2012.2189408.
[34] A.A. Sakellarios, C.V. Bourantas, L.S. Athanasiou, D.I. Fotiadis, L.K. Michalis, IVUS image processing methodologies, in: I.R.M. Association (Ed.), Image Processing: Concepts, Methodologies, Tools, and Applications, IGI Global, 2013, pp. 639–657, , https://doi.org/10.4018/978-1-4666-3994-2.ch033.
[35] M. Jourdain, J. Meunier, J. Sequeira, G. Cloutier, J.-C. Tardif, Intravascular ultrasound image segmentation: A helical active contour method, International conference on Image Processing Theory, Tools and Applications (IPTA), 2010, https://doi.org/10.1109/IPTA.2010.5586803.
[36] A. Hammouche, G. Cloutier, J.-C. Tardif, J. Meunier, Space curve approach for IVUS image segmentation, IEEE Life Sciences Conference (LSC), 2018, pp. 37–40, https://doi.org/10.1109/LSC.2018.8572073 2018.
[37] M. Kass, A. Witikin, D. Terzopoulos, Snakes: Active contour models, Int. J. Comput. Vis. 1 (4) (1988) 321–331, https://doi.org/10.1007/BF00133570.
[38] W. MathWorld, Helix, (1995) http://mathworld.wolfram.com/Helix.html , Accessed date: 1 November 2018.
[39] Y. Chen, T.S. Huang, Y. Rui, Optimal radial contour tracking by dynamic programming, Proceedings 2001 International Conference on Image Processing (Cat. No.01CH37205), vol. 1, 2001, pp. 626–629, , https://doi.org/10.1109/ICIP.2001.959123.
[40] M. Mignotte, J. Meunier, J.-C. Tardif, Endocardial boundary estimation and tracking in echocardiographic images using deformable templates and markov random fields, Pattern Anal. Appl. 4 (4) (2001) 256–271, https://doi.org/10.1007/PL00010988.
[41] E. Therasse, D. Donath, J. Lesprance, J.-C. Tardif, M.-C. Guertin, V.L. Oliva, G. Soulez, External beam radiation to prevent restenosis after superficial femoral artery balloon angioplasty, Circulation 111 (24) (2005) 3310–3315, https://doi.org/10.1161/CIRCULATIONAHA.104.502179.
[42] S. Balocco, C. Gatta, F. Ciompi, A. Wahle, P. Radeva, S. Carlier, G. Unal, E. Sanidas, J. Mauri, X. Carillo, T. Kovarnik, C.-W. Wangi, H.-C. Chen, T.P. Exarchos, D.I. Fotiadis, F. Destrempes, G. Cloutier, O. Pujol, M. Alberti, E.G. Mendizabal-Ruiz, M. Rivera, T. Aksoy, R.W. Downe, I.A. Kakadiaris, Standardized evaluation methodology and reference database for evaluating IVUS image segmentation, Comput. Med. Imag. Graph. 38 (2) (2014) 70–90, https://doi.org/10.1016/j.compmedimag.2013.07.001.
[43] D.P. Huttenlocher, G.A. Klanderman, W.J. Rucklidge, Comparing images using the hausdorff distance, IEEE Trans. Pattern Anal. Mach. Intell. 15 (9) (1993) 850–863, https://doi.org/10.1109/34.232073.
[44] V. Chalana, Y. Kim, A methodology for evaluation of boundary detection algorithms on medical images, IEEE Trans. Med. Imag. 16 (5) (1997) 642–652, https://doi.org/10.1109/42.640755.
[45] L.R. Dice, Measures of the amount of ecologie association between species, Ecology 26 (3) (1945) 297–302, https://doi.org/10.2307/1932409.
[46] P. Jaccard, Étude comparative de la distribution florale dans une portion des alpes et des jura, Bull. Soc. Vaudoise Sci. Nat. 37 (1901) 547–579.
[47] A. Baratloo, M. Hosseini, A. Negida, G.E. Ashal, Part 1: Simple definition and calculation of accuracy, sensitivity and specificity, Emergency 3 (2) (2015) 48–49, https://doi.org/10.22037/emergency.v3i2.8154.